Draft version November 3, 2021
Typeset using LaTeX **twocolumn** style in AASTeX631

An Imaging Search for Post-MS Companions of Sirius B

Miles Lucas [1], Michael Bottom [2], Garreth Ruane [3] and Sam Ragland [4]

[1] *Institute for Astronomy, University of Hawaii at Manoa, 2680 Woodlawn Dr, Honolulu, HI 96822, USA*
[2] *Institute for Astronomy, University of Hawaii at Hilo, 640 N Aohoku Pl, Hilo, HI 96720, USA*
[3] *Jet Propulsion Laboratory, California Institute of Technology, 4800 Oak Grove Dr, Pasadena, CA 91109, USA*
[4] *W.M. Keck Observatory, 65-1120 Mamalahoa Hwy, Waimea, HI 96743, USA*

ABSTRACT

Discovery and characterization of post-MS planets is essential to study planetary system evolution and planet-star interaction during the most critical phases of stellar evolution. We present deep imaging of Sirius B, the closest and brightest white dwarf, in order to constrain post-MS planetary evolution in the Sirius system. We use Keck/NIRC2 in L′-band (3.776 µm) across three epochs in 2020 using the technique of angular differential imaging. Our observations are contrast limited out to 1 AU and background limited beyond. The 5σ detection limits from our best performing epoch are 17 to 20.4 absolute magnitude. We consider multiple planetary formation pathways in the context of Sirius B's evolution to derive mass sensitivity limits using the ATMO2020 and Sonora Bobcat model grids. We achieve sub-Jupiter sensitivities and sub-AU separations, reaching $1.6\,M_J$ to $2.4\,M_J$ at 0.5 AU down to a sensitivity of $0.7\,M_J$ to $1.2\,M_J$ at >1 AU. Consistent with previous results, we do not detect any companions around Sirius B. Our excellent detection limits, even without coronagraphy, demonstrate the capabilities for modern high-contrast imaging studies of nearby (<25 pc) white dwarfs.

1. INTRODUCTION

In recent decades astronomers have discovered thousands of exoplanets orbiting stars that will eventually evolve into giants and then white dwarfs (Akeson et al. 2013). The fate of planets around these stars beyond the main-sequence (MS) is uncertain due to the large expansion, stellar winds, and high irradiation encountered on the giant branch (Veras 2016). Despite this, direct evidence from white dwarf (WD) pollution (Jura et al. 2007; Xu & Jura 2012), debris disks (de Ruyter et al. 2006; Zuckerman et al. 2010; Koester et al. 2014), and substellar companions (e.g., Luhman et al. 2011; Vanderburg et al. 2020; Blackman et al. 2021) culminate to suggest planetary systems beyond the MS are more common than previously thought. Discovery and characterization of post-MS planets is essential to study planetary system evolution and planet-star interaction during the most critical phases of stellar evolution.

The evolution of intermediate mass stars ($1\,M_\odot$ to $8\,M_\odot$) comprises a violent and relatively brief giant branch evolution before all nuclear fusion ends and the stars become WDs. As the MS star runs out of hydrogen to burn in its core, it will expand to 100s of times its size, engulfing any companions within the stellar radius. When helium fusion ignites the giant star becomes 3 to 4 orders of magnitude brighter than its MS progenitor, causing stellar winds and strong irradiation. Eventually the star will run out of fuel and conclude its nuclear burning and become a WD. The WD begins cooling, becoming 3 to 4 orders of magnitude dimmer than its MS progenitor.

There is limited knowledge of planetary systems around evolved stars. The pathway for a *first-generation* planet around a post-MS host is violent and uncertain. For a planet to survive the giant branch evolution, it first needs to escape engulfment as well as tidal shredding (Burleigh et al. 2002; Nordhaus & Spiegel 2013). Surviving planets are subject to adiabatic orbit expansion (Jeans 1924), which can potentially de-stabilize multi-object systems, stellar winds, and high irradiation which enriches the circumstellar environment with metals and dust, and strongly heats planets close to the giant star (Mustill & Villaver 2012; Veras 2016). The expansion and tidal effects on the circumstellar environment create a "forbidden" region of exoplanet phase space for orbital separations closer than ∼5 AU.

Corresponding author: Miles Lucas
mdlucas@hawaii.edu

Recent discoveries of exoplanets in "forbidden" formation regions (Vanderburg et al. 2020; Blackman et al. 2021) suggest evidence for a class of *second-generation* companions. Perets (2010, 2011) describe a planetary formation pathway where in multi-star systems the stellar ejecta from an evolving giant star forms a protoplanetary disk around a separate star (or, in fact, the whole system). Such disks would have lifetimes of 1 Myr to 100 Myr which is commensurate with "hot-start" planetary formation timescales (Spiegel & Burrows 2012). A first-generation planet could act as a seed for planetesimal growth in these disks, too. Another formation pathway considers the chaotic evolution of companion orbits due to stellar mass loss in the presence of multiple bodies. Perets & Kratter (2012) describe this interaction for triplet systems in detail (the "triple evolution dynamical interaction", or TEDI). Kratter & Perets (2012) explore similar dynamical interactions in the restricted 3-body problem and concluded up to ∼10% of all WD binaries might contain "star-hopper" planets which migrate between the stars.

Previous searches for substellar companions around white dwarfs (e.g., Debes & Sigurdsson 2002; Hogan et al. 2009; Luhman et al. 2011; Xu et al. 2015) have primarily focused on detecting wide-orbit planets which survived the giant branch evolution of their hosts. We posit that previously "forbidden" regions of planetary evolution are worth investigating by utilizing the modern high-contrast instrumentation that has come to fruition in the recent decade. In the rest of this report, we will discuss high-contrast imaging as a detection technique for post-MS systems (Section 2). We will introduce the Sirius system as a potential candidate for post-MS companions, along with previous studies of WD Sirius B (Section 3). We will detail our 2020 near-infrared observations of Sirius B with Keck/NIRC2, as well as our processing steps and statistical analysis for companion detection (Section 4, Section 5). Lastly, we will discuss our results within the context of Sirius and post-MS systems as well as future directions for post-MS imaging (Section 6, Section 7).

2. DIRECTLY IMAGING POST-MS SYSTEMS

High-contrast imaging is a powerful technique for discovering and characterizing exoplanets. Directly imaging a circumstellar companion is difficult, though. The typical astrophysical flux ratios (contrasts) for a Sun-Jupiter analog in the near-infrared (NIR) are $\sim 10^{-8}$, and for a Sun-Earth system are $\sim 10^{-10}$ (Traub & Oppenheimer 2010). In addition, the close angular separations of planets make it difficult to detect them over the diffraction pattern of their host and other noise sources. Thermal emission from exoplanets peaks, well into in the infrared, on the Rayleigh-Jeans limit of the stellar spectrum. This makes infrared observations preferred over optical or ultraviolet observations due to the reduced contrast.

WDs are interesting targets for direct imaging- they are 3 to 4 orders of magnitude fainter than their MS progenitors which reduces the contrast necessary to detect a companion. The high effective temperatures of WD photospheres pushes the peak thermal emission even further into the optical and ultraviolet, reducing the intrinsic contrast between the star and the planet. In addition, the lack of spectral features of WDs (Schatzman 1945) makes them imprecise targets for the radial velocity technique. The faintness of WDs proves challenging due to the high signal-to-noise ratio (S/N) required by modern adaptive optics (AO) instruments. This is exacerbated on ground-based telescopes which require extreme AO to counteract the effects of atmospheric seeing. This constrains potential companion searches to relatively bright targets ($m^R \lesssim 13$). Implicitly, this also limits searches to nearby WDs ($d \sim 25$ pc, Holberg et al. 2016), which is beneficial for imaging because the limited inner working angle of the instrumentation will project to closer separations around closer stars.

3. SIRIUS B AND THE SIRIUS SYSTEM

One fascinating target for post-MS observations is Sirius B, the closest and brightest WD to our solar system. The Sirius system is the 7th closest to the sun at 2.7 pc, consisting of Sirius A, a -1.35 magnitude A1V star and Sirius B, a DA white dwarf with a 50 yr orbit (Collaboration et al. 2016; Bond et al. 2017; Collaboration et al. 2021). As mentioned previously, the proximity and faintness of Sirius B (compared to a MS star) make it compelling for direct imaging. Additionally, the young system age (∼225 Myr) means any giant planets would still retain much of their latent formation heat, increasing their luminosity in the IR (Fortney et al. 2010).

Sirius is one of the oldest studied star systems; the breadth and depth of knowledge about the binary gives exceptional precision for characterizing the circumstellar environment. Initial astrometric measurements suggested a 50 year orbital period for Sirius B (Auwers 1864). Most recently, Bond et al. (2017) used Hubble Space Telescope (HST) along with old photographic plates to compile the most precise orbital solution for Sirius, to date. They derived dynamical masses using their orbital solution and Hipparcos parallaxes: $(2.063 \pm 0.023)\,M_\odot$ and $(1.018 \pm 0.011)\,M_\odot$ for A and B, respectively. A companion around Sirius B would be affected by the orbit of Sirius A, and this constrained

three-body system has been studied numerically (Holman & Wiegert 1999). Bond et al. (2017) calculate the longest period stable companion around Sirius B is 1.79 yr, which corresponds to a 1.5 AU circular orbit.

The total age of Sirius B is the combination of its WD cooling age and the time from the zero-age MS (ZAMS) to the tip of the giant branch (TGB). We adapt the cooling age derived by Bond et al. (2017, sec. 8) of 126 Myr. We use the updated WD initial-final mass relation (IFMR) of Cummings et al. (2018) to estimate the Sirius B progenitor mass of $(5.1 \pm 1.1)\,M_\odot$.

We adopt the system age derived in Cummings et al. (2018) using MIST isochrones of 225 Myr, which implies a ZAMS to TGB age of 99 Myr. These age determinations are limited both by the precision of the stellar parameters as well as the stellar evolution model. The spread of ages derived by Cummings et al. (2018) from different models is ∼10 Myr. An age uncertainty of ∼4% is exceptional compared to the ∼10% or worse of stars found in young moving groups, not to mention many stars cannot be precisely dated at all. These values are compiled in Table 1.

One of the peculiarities of the Sirius system is its large eccentricity of 0.59 (Bond et al. 2017). If we assume the orbital expansion due to Sirius B's evolution was adiabatic, we can calculate the initial semi-major axis of the binary

$$a_i = a_f \frac{M_{B,f} + M_{A,f}}{M_{B,i} + M_{A,i}} \tag{1}$$

where a is the system semi-major axis, M_A and M_B are the respective stellar masses, and subscripts i and f correspond to the initial (MS) versus final (post-MS) states. The current semi-major axis of the binary is 20 AU, and assuming negligible mass transfer between the two stars, the initial semi-major axis would be (8.6 ± 1.3) AU. If the orbit expansion was indeed adiabatic, the eccentricity would be the same before and after evolution. In this case, the periastron of Sirius A and B would be (3.52 ± 0.52) AU. Veras (2016) tabulated the maximum stellar radius of intermediate mass stars during their giant evolution, from which we interpolate a maximum radius for Sirius B of (5.104 ± 0.075) AU. This means Sirius A certainly interacted with Sirius B and may have had a common envelope stage. Mass transfer and tidal circularization would be expected, however the present-day eccentricity provide contrary evidence.

Bonačić Marinović et al. (2008) propose an explanation for the lack of tidal circularization called "tidal-pumping", but neglect to address the observed slow rotation speed of Sirius A (Gray 2014; Takeda 2020), which we would expect to increase with mass transfer to conserve total angular momentum in the binary. Perets & Kratter (2012) suggest the present eccentricity could be due to the chaotic expulsion of third body between $0.6\,M_\odot$ to $5.5\,M_\odot$. Kratter & Perets (2012) point out, though, that the most probable outcome of a planetary-mass companion in a chaotic orbital evolution is collision with one of the binary components. We extrapolate their Figure 7 using the parameters for Sirius to estimate a ∼70% collision probability for an initial companion of Sirius B if it is chaotically ejected. When combined, these studies show the necessity to consider multiple, potentially exotic formation pathways for planetary candidates.

We also consider adiabatic orbit expansion of a substellar companion

$$a_i = a_f \frac{M_f}{M_i} \tag{2}$$

where a is the semi-major axis, and M is the stellar mass of Sirius B. Using the maximum stellar radius of (5.104 ± 0.075) AU and assuming an extra 20% separation to escape tidal shredding (Nordhaus & Spiegel 2013) would create a forbidden region within (31 ± 6) AU around present Sirius B. In combination with the dynamical stability limits of 1.5 AU, we can readily rule out the plausibility of detecting a first-generation companion of Sirius B.

There have been many attempts to find planets in the Sirius system, but so far no planets have been detected. Benest & Duvent (1995) suggested the presence of a third body with astrometric perturbations of 100 mas, but this has so far been unrealized, with Bond et al. (2017) reducing astrometric uncertainty down to ∼10 mas. The first modern imaging study searching for companions around Sirius B was Schroeder et al. (2000) who used the HST wide-field planetary camera (WFPC) at 1 µm. Around the same time Kuchner & Brown (2000) searched in a narrower field of view (FOV) with HST/NICMOS at 1 µm. A planetary atmosphere and evolution model are needed in order to derive mass sensitivity limits from imaging. Prior works to our own do not necessarily make the same model choices that we do (Section 6) biasing direct comparisons of mass limits. These studies combined reported sensitivities down to ∼10 M_J at 5.3 AU (2″). Bonnet-Bidaud & Pantin (2008) used the ground-based ESO/ADONIS instrument in J, H, and Ks-band and reported a sensitivity of ∼30 M_J at 7.9 AU (3″). Skemer & Close (2011) used mid-IR (up to 10 µm) observations from Gemini/T-ReCs, which ruled out evidence for significant infrared excess from massive disks around Sirius B. Thalmann et al. (2011) used Subaru/IRCS at 4.05 µm reporting sensitivities of 6 M_J to

Table 1. Parameters of the Sirius system adopted in this study.

parameter	value	unit	ref.
$t_{\rm sys}$	225	Myr	B17; C18
π	374.49 ± 0.23	mas	G21a
d	2.6702 ± 0.0016	pc	G21a
a	20.016 ± 0.014	AU	B17
Sirius A			
$M_\star$	2.063 ± 0.023	$M_\odot$	B17
Sirius B			
$M_\star$	1.018 ± 0.011	$M_\odot$	B17
$M_{\rm MS}$	5.1 ± 1.1	$M_\odot$	B17; C18
$t_{\rm WD}$	126	Myr	B17
$m^{\rm L'}$	9.1 ± 0.2		BB08
$M^{\rm L'}$	11.97 ± 0.20		BB08; G21a

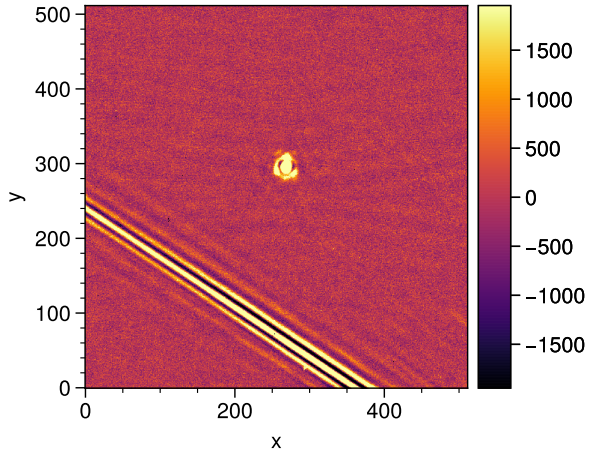

Figure 1. Scattered light from Sirius A is present in our FOV around Sirius B as shown by this diffraction spike sweeping across a calibrated science frame of Sirius B from the first epoch. Despite Sirius B's separation of 11″, the overwhelming brightness of Sirius A impedes observations of Sirius B.

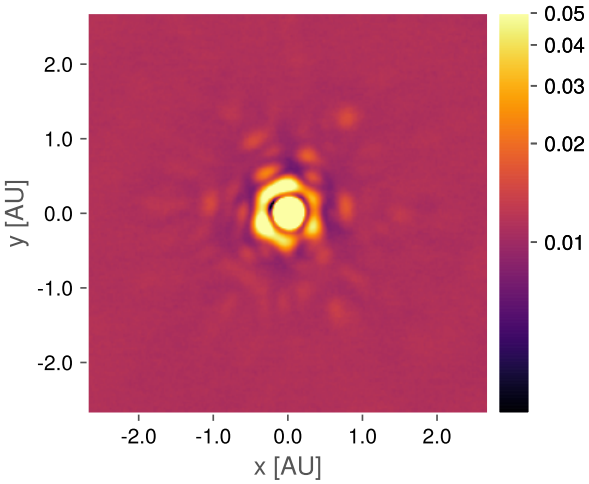

Figure 2. The median frame from the second epoch showing the instrumental PSF. The inner core has a Gaussian FWHM of ∼76 mas. The blobs surrounding the first ring are the speckles, with roughly 6-way radial symmetry coinciding with the hexagonal shape of the primary mirror.

$12\,M_J$ at 1″. Recently, Pathak et al. (2021) took coronagraphic mid-IR observations (10 µm) at VLT/VISIR of Sirius A which contained Sirius B in the FOV. Because of the simultaneous observation, their contrast had an azimuthal dependence. Their average reported sensitivity is $\sim 2.5\,M_J$ at 1 AU, and their best sensitivity (from the "inner" region) is $\sim 1.5\,M_J$ at 1 AU.

4. OBSERVATIONS

We directly imaged Sirius B with Keck/NIRC2 in L′-band (3.776 µm) using the narrow camera (10 mas px^{-1}; 2.5″×2.5″) across three epochs in 2020 (Table 2). Despite Sirius B being the brightest white dwarf in the sky, it is still 10 magnitudes fainter than Sirius A, making it a technically challenging target, especially on ground-based telescopes. Our first attempt to observe Sirius B failed due to the strong scattered light from Sirius A. The adaptive optics (AO) calibration failed when the scattered light from Sirius A would sweep into the FOV of the wavefront sensor (WFS). Similarly, trying to deploy the focal-plane vortex coronagraph (Serabyn et al. 2017) failed when the coronagraphic pointing control algorithm, `QACITS` (Huby et al. 2017), performed erratically in the presence of the scattered light. We did not try coronagraphy for the remaining observations. Vigan et al. (2015, §2) reported similar issues in their attempts to image Sirius B coronagraphically using VLT/SPHERE. In order to overcome these obstacles, we decided to used Sirius A as the AO guide star and off-axis guided on Sirius B.

The Keck facility AO system (Wizinowich et al. 2000) was saturated by Sirius A, so we attenuated the flux using a narrow laser-line filter in the WFS. While still bright (appearing like a ∼5 magnitude star on the WFS), this was enough attenuation to close the AO loop. From here, we slewed off-axis using the separa-

Table 2. Observing parameters for the three epochs of data. All observations were carried out using the NIRC2 narrow camera ($10\,\mathrm{mas\,px^{-1}}$; $2.5''\times2.5''$) in L′-band ($3.776\,\mu\mathrm{m}$). Observation time is based on the frames that were selected for processing. Seeing values were measured at $0.5\,\mu\mathrm{m}$ using a differential image motion monitor and averaged over the observing session. Seeing values, temperature, and water vapor measurements were all retrieved from the Maunakea weather center forecast archive.

Date observed	Sirius B offset ($''$)	Sirius B PA ($^\circ$)	Obs. time (hr)	FOV rotation ($^\circ$)	FWHM (mas)	Seeing ($''$)	Temp (°C)	PWV (mm)
2020-02-04	11.20	67.90	1.44	60.1	79.9	0.936	0.0	0.7
2020-11-21	11.27	66.42	2.91	91.4	76.4	0.871	0.8	3.5
2020-11-28	11.27	66.38	2.44	80.4	82.2	1.23	-1.5	3.0

tions and position angles calculated in Table 2 from the orbital solution of Bond et al. (2017). In this mode, we noticed higher than usual drift in the focal plane, requiring manually recentering the target every 5 or 10 minutes.

During each observation, we took dark frames and sky-flat frames for calibration. All observations used the large hexagonal pupil mask and set the telescope's field rotator to track the pupil in order to exploit the natural rotation of the sky via angular differential imaging (ADI; Marois et al. 2006). In order to avoid saturation from the sky background, we used 0.4 s integration times and coadded every 75 acquisitions, resulting in ∼30 s per frame in the final images.

5. ANALYSIS

5.1. *Pre-processing*

The raw images from NIRC2 required pre-processing before analyzing them for companions. For each epoch, we applied a flat correction using calibration frames captured during observing. We also removed bad pixels using a combination of `L.A.Cosmic` (van Dokkum 2001) and an adaptive sigma-clipping algorithm. We removed sky background using a high-pass median filter with a box size of 31 pixels. For both the November epochs we tried exploiting the large focal plane drifts by dithering between two positions in order to simplify background subtraction, but this ended up performing worse than the high-pass filter. At this point frames were manually selected to remove bad frames, especially those with diffraction spikes from Sirius A within a few hundred pixels, like in Figure 1. Then, each selected frame was co-registered to sub-pixel accuracy using the algorithm presented in Guizar-Sicairos et al. (2008), followed by fitting each frame with a Gaussian PSF to further increase centroid accuracy.

The co-registered frames were shifted to the center of the FOV and cropped to the inner 200 pixels. With a pixel scale of 10 mas, the crop corresponds to a maximum separation of $1''$ or a projected separation of 2.7 AU. All the frames were stacked into data cubes for each epoch. We also measure the parallactic angle of each frame, including corrections for distortion effects following Yelda et al. (2010). For each epoch, we measure the full-width at half-maximum (FWHM) of the stellar PSF for use in post-processing by fitting a bivariate Gaussian model to the median frame from each data cube (Figure 2). All of the pre-processing code is available in Jupyter notebooks in a GitHub repository (Section 8).

5.2. *Post-processing*

By taking data with the field rotator disabled (ADI), the point-spread function (PSF) will not appear to rotate while any potential companion will appear to rotate. This reduces the probability of removing companion signal when we subtract the stellar PSF model. After subtraction, the frames are derotated by their parallactic angle and combined with a weighted sum (Bottom et al. 2017), which reduces the pixel-to-pixel noise as the number of frames in the data cube increases.

For this analysis, we used four ADI algorithms for modeling and subtracting the stellar PSF: median subtraction (Marois et al. 2006), principal component analysis (PCA, also referred to as KLIP; Soummer et al. 2012), non-negative matrix factorization (NMF; Ren et al. 2018), and fixed-point greedy disk subtraction (GreeDS; Pairet et al. 2019b, 2020). The median subtraction and PCA methods were also applied in an annular method, where we modeled the PSF in annuli of increasing separation, discarding frames that have not rotated at least 0.5 FWHM (Marois et al. 2006). These algorithms are implemented in the open-source `ADI.jl` Julia package (Lucas & Bottom 2020).

We determined the best performing PSF subtraction algorithm by measuring the throughput of companion signal through repeated injection and recovery. By using a known, fixed S/N for injection, the 5σ detection limits can be measured at various positions within the

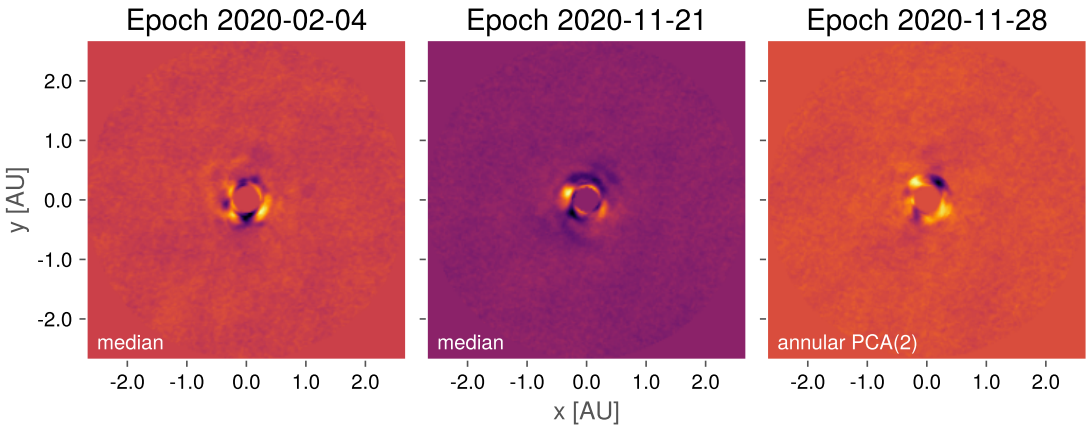

Figure 3. The flat residuals of each epoch after PSF subtraction, derotating, and collapsing. The inner two FWHMs are masked out for each frame.

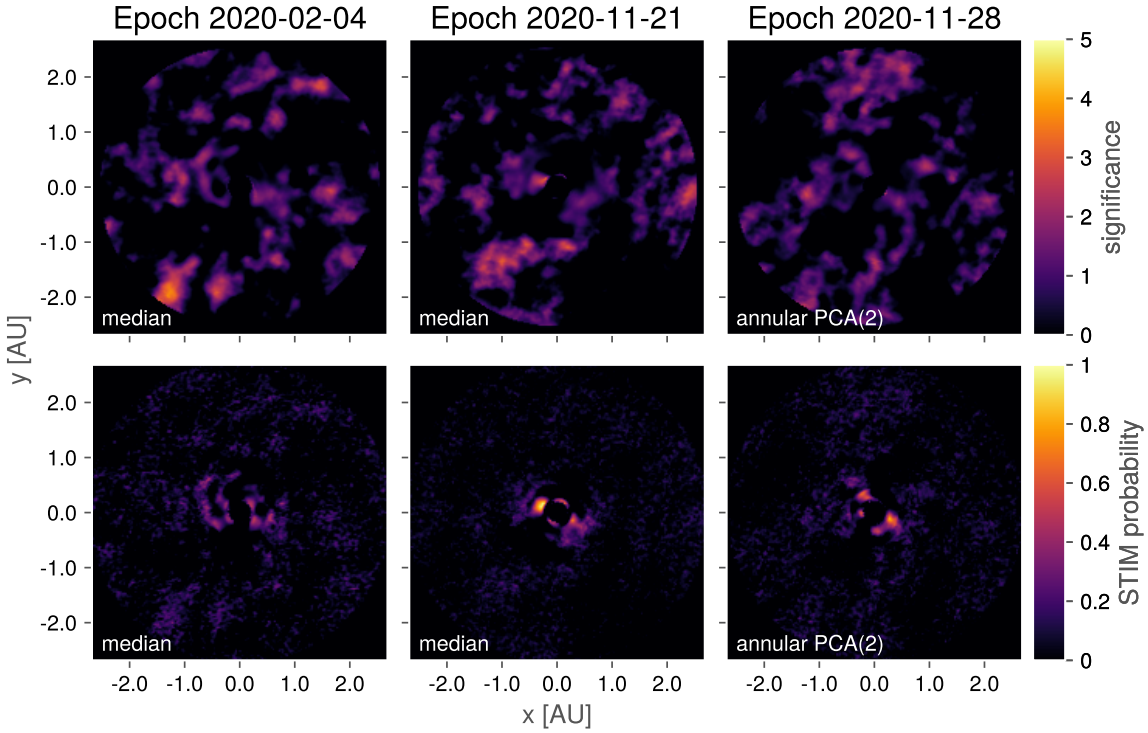

Figure 4. top row: The *significance* maps for each epoch accounting for small-sample statistics (Mawet et al. 2014). Typically a critical value for detection is 5. **bottom row:** The STIM maps for each epoch calculated from each residual cube. The STIM probability has a typical cutoff threshold of 0.5 for significant detections. The inner two FWHMs are masked out for each map.

FOV and are azimuthally averaged to produce a *contrast curve*. We calculate both the Gaussian contrast and the Student-t corrected contrast, which accounts for the small-sample statistics in each annulus (Mawet et al. 2014). We employed two different detection metrics to search for companions in the residual data: the Gaussian significance map (Mawet et al. 2014) and the standardized trajectory intensity mean map (STIM map; Pairet et al. 2019a). These maps assign the likelihood of a companion to each pixel using different assumptions of the residual statistics. These three metrics are calculated using the methods available in `ADI.jl`. The collapsed residual frames along with the above metrics for each algorithm and epoch are in Appendix A.

A common problem when using subspace-driven post-processing algorithms like PCA, NMF, or GreeDS is choosing the size of the subspace (i.e., the number of components). For PCA, NMF, and GreeDS algorithms,

we varied the number of components from 1 to 10, creating a residual cube for each iteration. We chose 10 for the maximum number of components because we saw a dramatic decline in contrast sensitivity after the first few components (Figure 12). In our analysis we employed the STIM largest intensity mask map (SLIM map; Pairet 2020) as an ensemble statistic. The SLIM map calculates the average STIM map from many residual cubes along with the average mask of the N most intense pixels in each STIM map. A real companion ought to be present in many different residual cubes from the same dataset, so this ensemble approach can give us a probability map without predetermining the number of components. The collapsed residual frames, average STIM map, SLIM map, and contrast curves for each epoch for each of the above algorithms are in Appendix A. All of the code used for this analysis is available in a GitHub repository (Section 8).

6. RESULTS

We determined the best-performing algorithms for each epoch using the contrast curves described in Section 5. For the first two epochs, full-frame median subtraction had the best contrast at almost all separations. For the last epoch annular PCA subtraction with 2 principal components and a rotation threshold of 0.5 FWHM produced the best contrast at close separations (0.2″ to 0.4″) and had similar performance to other algorithms beyond 0.4″. This algorithm was unable to detect a 100 S/N companion injected into the innermost annulus with 5σ significance. The contrast for this innermost annulus is therefore not plotted. Figures 3 to 4 show the collapsed residual frames from each epoch, along with the Gaussian significance maps and STIM maps.

We show the contrast curves from the best performing algorithm for each reduction in Figure 5. We determine the limiting sensitivities in terms of the planetary mass by first calculating the contrast-limited absolute magnitude using an L′-band magnitude for Sirius B of 9.1 (adapted from Ks-band magnitude from Bonnet-Bidaud & Pantin 2008) and a distance modulus of −2.87 (Collaboration et al. 2021). We divide Figure 5 into two regimes: speckle-limited and background-limited. The speckle-limited regime exists from 0.2 AU to 1 AU characterized by the increasing sensitivity with separation. Here we reach a median 5σ detection limit of ∼19 magnitude (L′). This regime is constrained by the quality of the AO correction and the PSF subtraction method, mainly. The background-limited regime (>1 AU) is characterized by the flattening of the contrast curves, and is primarily constrained by the sky brightness. In this region, we reach 20.4 magnitude (L′) in the 2020-11-21 epoch. Our data is background-limited due to the relative brightness of the sky in L′(2.91 mag/sq arcsec[1]) compared to the pixel-to-pixel noise sources (e.g., read noise).

6.1. *Companions around Sirius B*

The reduced images do not show consistent or significant evidence for a substellar companion. The STIM probability maps for the 2020-11-21 and 2020-11-28 epochs suggest evidence for some blobs ∼0.3 AU (0.13″; 1.6 FWHM) from the center. The February epoch also shows a blob at a similar separation in the reduced image which does not appear in the STIM map. The lack of statistical evidence in the February epoch and the significance maps as well as the proximity to the central star both reduce the probability of these blobs being true companions. Nonetheless, we estimated astrometry for blobs from each epoch (Table 3) and tried fitting Keplerian orbits using the "Orbits for the Impatient" algorithm (OFTI; Blunt et al. 2017). We generated 10^4 orbits, none of which constrained the points from each epoch (Appendix B). This implies non-Keplerian motion and we take this as direct evidence against the blobs being substellar companions of any kind. The signal can be simply explained as residual starlight not removed during PSF subtraction.

6.2. *Mass detection limits*

In order to convert our photometric detection limits to mass limits we must employ an appropriate planetary atmosphere model and evolution grid. This is not a trivial task, as the effects of post-MS stellar evolution on planets are highly uncertain and not readily modeled in the currently available grids. In particular, we want to study the effects of metal and dust enrichment of the circumstellar environment from stellar winds. We start with the ATMO2020 model grid (Phillips et al. 2020) for our solar metallicity model. Following Pathak et al. (2021), we use the non-equilibrium chemistry models with weak vertical mixing, which model very cool objects better than previous grids such as AMES-Cond (Allard et al. 2012). The ATMO2020 models are not available for non-solar metallicities, yet, so we also employ the Sonora Bobcat grid (Marley et al. 2021a,b) at both solar and +0.5 dex metallicity.

To determine the correct isochrone for the grids, we consider two formation scenarios. If a first-generation planet survives the giant phase of Sirius B through star hopping, it would have an age closer to the system age of 225 Myr. If the planet formed in a disk of stellar ejecta

[1] https://www2.keck.hawaii.edu/inst/nirc2/sensitivity.html

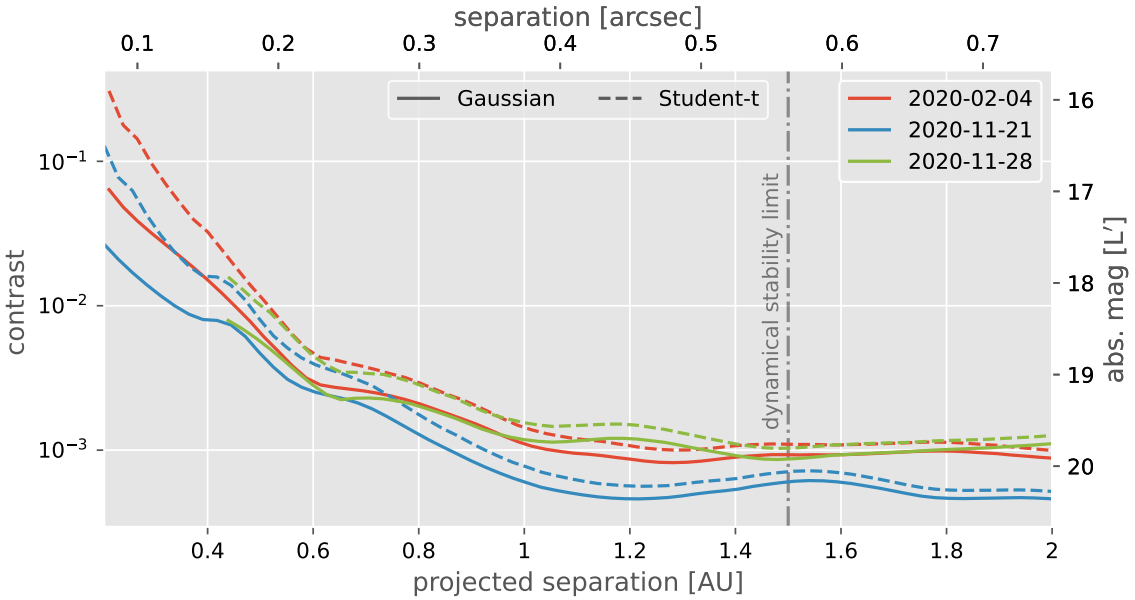

Figure 5. The contrast curves for the best performing algorithm from each epoch. The solid lines are the Gaussian 5σ contrast curves and the dashed lines are the Student-t corrected curves. The absolute magnitude are calculated using an absolute magnitude for Sirius B of 11.97. The expected upper limit for a dynamically stable orbit of 1.5 AU is plotted as a vertical dashed line. The annular PCA curve cuts off because the innermost annulus was not able to detect a 100 S/N companion with 5σ significance.

during the AGB phase, the age would be closer to the WD cooling age of 126 Myr. If the planet formed in such a disk, or if it accreted some of the material, it would almost certainly have peculiar chemistry, although it is uncertain exactly how the relative abundances would change.

Figure 6 shows our most sensitive contrast curve converted to mass limits under the different models. The first panel uses the ATMO2020 models to show how the choice of isochrone age leads to a $\sim$0.3 M_J difference in the background-limited regime. The second panel uses the Sonora models to demonstrate the relatively minor effects ($\sim$0.1 M_J) the increased metallicity has on the mass limits. We could not fully utilize the Sonora grid, though, because there are no atmospheric models tabulated for effective temperatures below 200 K, which are precisely the models we need for the background-limited regimes. Overall, we constrain our detection limits to 1.6 M_J to 2.4 M_J at 0.5 AU (0.19″) in the speckle-limited regime and ultimately 0.7 M_J to 1.1 M_J at >1 AU (0.38″) in the background-limited regime.

7. DISCUSSION & CONCLUSIONS

Post-MS planetary evolution has historically been limited to theoretical work. Recently, though increasingly strong and diverse observational constraints have invigorated the field. We set out in this work to study the nearby Sirius system for post-MS companions around Sirius B. The Sirius system is one of the most well studied in history, with Sirius B being the target of companion searches from the visible to the IR. While it is highly unlikely a first-generation planet survived post-MS evolution, imaging efforts have gradually increased the sensitivity to second-generation planets. In this work, we presented high-contrast images of Sirius B in the near-IR. Our 5σ sensitivity limits are the best that have been reached for Sirius B so far, reaching 20.4 L′absolute magnitude at >1 AU. We consider multiple planetary formation pathways yielding ages between 126 Myr to 225 Myr and explore the effects of enriched metallicity. We translate our sensitivity limits using the ATMO2020 and Sonora Bobcat grids to constrain our mass detection limits to 0.7 M_J to 1.1 M_J at >1 AU. Our observations also show how the high precision of the parameters of the Sirius system directly benefits the sensitivity to planets. For example, the $\sim$4% relative uncertainty of Sirius B's age translates to mass detection limit uncertainty below 0.1 M_J. Despite the high sensitivity of this study, we found no significant evidence for a companion around Sirius B, consistent with previous results.

Although our observations yield no detections, we illustrate the capability of modern high-contrast instrumentation, even without coronagraphy, to reach exceptional detection limits. We took the WD sample from Holberg et al. (2016) and analyzed the 7 binary systems. The median distance of this subset is 20 pc. In

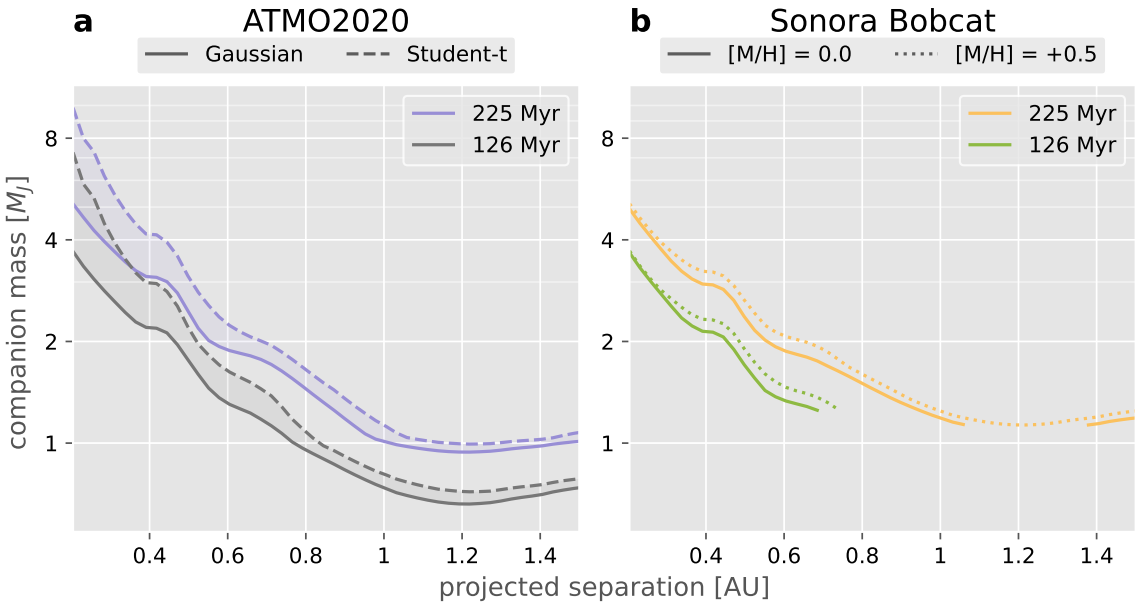

Figure 6. Mass sensitivity curves derived from the 2020-11-21 epoch, which has the most sensitive contrast. The limits are calculated from the absolute magnitude derived in the contrast curves. Both curves are truncated at 1.5 AU due to the dynamical stability limit. **(a)** The absolute magnitudes are converted to masses using the ATMO2020 isochrone grid with non-equilibrium chemistry and weak convective mixing. The solid lines are the Gaussian 5σ detection limits and the dashed lines are the Student-t corrected limits. The two ages represent the ages of two potential formation pathways, one of which is the system age (225 Myr), the other is the WD cooling age of Sirius B (126 Myr). The relative difference between the ages comes out to $\sim$0.3 M_J at 1 AU. **(b)** The absolute magnitudes are converted to masses using the Sonora Bobcat grid with solar metallicity (solid lines) and with +0.5 dex metallicity (dotted lines). For clarity, we only show the Gaussian contrast curves in this panel. The Sonora grid does not have atmospheric spectra for $T_{\rm eff}$ <200 K, which causes the cutoffs around 1 M_J. The relative difference due to the metallicity is $\sim$0.1 M_J.

this work, our inner working angle due to the stellar PSF was $\sim$80 mas, which would be a projected separation of 1.6 AU at 20 pc. The median R magnitude is $\sim$15.2, though, which may prove challenging for natural guide star AO. However, with laser guide stars (LGS; e.g., van Dam et al. 2006; Baranec et al. 2018), the limiting magnitude increases significantly ($m^R \lesssim 19$). We suspect future work using LGS AO is capable of studying WD systems at the sub-AU and sub-Jupiter-mass scales. Such observations could significantly improve our theories of planetary formation and stellar evolution beyond the MS.

We also consider future space-based observations with the James Webb Space Telescope (JWST), eliminating the effects of atmospheric seeing and the bright sky background. For example, using JWST/NIRCAM in long-wavelength imaging mode has a limiting magnitude of $\sim$25 in the F480M filter. The pixel scale ($0.06''\,{\rm px}^{-1}$) and PSF size ($\sim$0.3″) are adequate for sub-AU observations of nearby WDs, depending on the contrast-limited performance of NIRCAM. Unfortunately, Sirius B is far too bright and too close to Sirius A to observe with JWST without severe saturation.

8. DATA AND CODE AVAILABILITY

All of the code used for pre-processing data, reducing data, and generating the figures is available under an open-source license in a GitHub repository.[2] This code includes all of the scripts for generating each figure in this manuscript. The pre-processed data cubes and parallactic angles are available on Zenodo under an open-source license.[3] We hope that this improves the reproducibility of the work as well as providing data for future investigations. Please reach out to the corresponding author for further inquiries regarding data and code availability.

[2] https://github.com/mileslucas/sirius-b
[3] 10.5281/zenodo.5115225

ACKNOWLEDGMENTS

We thank the anonymous referee for their helpful comments. We thank Michael Liu and Mark Phillips for their expertise and advice on the ATMO2020 model grid. We thank Mark Marley and Didier Saumon for their assistance with the Sonora Bobcat model grid. The data presented herein were obtained at the W. M. Keck Observatory, which is operated as a scientific partnership among the California Institute of Technology, the University of California, and the National Aeronautics and Space Administration. The Observatory was made possible by the generous financial support of the W. M. Keck Foundation. The authors wish to recognize and acknowledge the very significant cultural role and reverence that the summit of Maunakea has always had within the indigenous Hawaiian community. We are most fortunate to have the opportunity to conduct observations from this mountain.

Facility: Keck:II (NIRC2)

Software: ADI.jl (Lucas & Bottom 2020), astropy (Collaboration et al. 2013; Astropy Collaboration et al. 2018), Julia (Bezanson et al. 2017), numpy (Harris et al. 2020), scikit-image (Walt et al. 2014),

REFERENCES

Akeson, R. L., Chen, X., Ciardi, D., et al. 2013, Publications of the Astronomical Society of the Pacific, 125, 989, doi: 10.1086/672273

Allard, F., Homeier, D., & Freytag, B. 2012, Philos Trans A Math Phys Eng Sci, 370, 2765, doi: 10.1098/rsta.2011.0269

Astropy Collaboration, Price-Whelan, A. M., Sipőcz, B. M., et al. 2018, The Astronomical Journal, 156, 123, doi: 10.3847/1538-3881/aabc4f

Auwers, A. 1864, Monthly Notices of the Royal Astronomical Society, 25, 38. https://ui.adsabs.harvard.edu/abs/1864MNRAS..25...38A

Baranec, C., Chun, M., Hall, D., et al. 2018, 10703, 1070327, doi: 10.1117/12.2312835

Benest, D., & Duvent, J. L. 1995, Astronomy and Astrophysics, 299, 621. https://ui.adsabs.harvard.edu/abs/1995A&A...299..621B/abstract

Bezanson, J., Edelman, A., Karpinski, S., & Shah, V. B. 2017, SIAM Rev., 59, 65, doi: 10.1137/141000671

Blackman, J. W., Beaulieu, J. P., Bennett, D. P., et al. 2021, Nature, 598, 272, doi: 10.1038/s41586-021-03869-6

Blunt, S., Nielsen, E. L., De Rosa, R. J., et al. 2017, The Astronomical Journal, 153, 229, doi: 10.3847/1538-3881/aa6930

Bonačić Marinović, A. A., Glebbeek, E., & Pols, O. R. 2008, Astronomy and Astrophysics, 480, 797, doi: 10.1051/0004-6361:20078297

Bond, H. E., Schaefer, G. H., Gilliland, R. L., et al. 2017, The Astrophysical Journal, 840, 70, doi: 10.3847/1538-4357/aa6af8

Bonnet-Bidaud, J.-M., & Pantin, E. 2008, A&A, 489, 651, doi: 10.1051/0004-6361:20078937

Bottom, M., Ruane, G., & Mawet, D. 2017, Research Notes of the American Astronomical Society, 1, 30, doi: 10.3847/2515-5172/aa9d18

Burleigh, M. R., Clarke, F. J., & Hodgkin, S. T. 2002, Monthly Notices of the Royal Astronomical Society, 331, L41, doi: 10.1046/j.1365-8711.2002.05417.x

Collaboration, A., Robitaille, T. P., Tollerud, E. J., et al. 2013, Astronomy and Astrophysics, 558, A33, doi: 10.1051/0004-6361/201322068

Collaboration, G., Prusti, T., de Bruijne, J. H. J., et al. 2016, Astronomy and Astrophysics, 595, A1, doi: 10.1051/0004-6361/201629272

Collaboration, G., Brown, A. G. A., Vallenari, A., et al. 2021, Astronomy and Astrophysics, 649, A1, doi: 10.1051/0004-6361/202039657

Cummings, J. D., Kalirai, J. S., Tremblay, P. E., Ramirez-Ruiz, E., & Choi, J. 2018, The Astrophysical Journal, 866, 21, doi: 10.3847/1538-4357/aadfd6

de Ruyter, S., van Winckel, H., Maas, T., et al. 2006, Astronomy and Astrophysics, 448, 641, doi: 10.1051/0004-6361:20054062

Debes, J. H., & Sigurdsson, S. 2002, The Astrophysical Journal, 572, 556, doi: 10.1086/340291

Fortney, J. J., Baraffe, I., & Militzer, B. 2010, Giant Planet Interior Structure and Thermal Evolution. https://ui.adsabs.harvard.edu/abs/2010exop.book..397F

Gray, D. F. 2014, The Astronomical Journal, 147, 81, doi: 10.1088/0004-6256/147/4/81

Guizar-Sicairos, M., Thurman, S. T., & Fienup, J. R. 2008, Opt. Lett., OL, 33, 156, doi: 10.1364/OL.33.000156

Harris, C. R., Millman, K. J., van der Walt, S. J., et al. 2020, Nature, 585, 357, doi: 10.1038/s41586-020-2649-2

Hogan, E., Burleigh, M. R., & Clarke, F. J. 2009, Monthly Notices of the Royal Astronomical Society, 396, 2074, doi: 10.1111/j.1365-2966.2009.14565.x

Holberg, J. B., Oswalt, T. D., Sion, E. M., & McCook, G. P. 2016, Monthly Notices of the Royal Astronomical Society, 462, 2295, doi: 10.1093/mnras/stw1357

Holman, M. J., & Wiegert, P. A. 1999, The Astronomical Journal, 117, 621, doi: 10.1086/300695

Huby, E., Bottom, M., Femenia, B., et al. 2017, Astronomy and Astrophysics, 600, A46, doi: 10.1051/0004-6361/201630232

Jeans, J. H. 1924, Monthly Notices of the Royal Astronomical Society, 85, 2, doi: 10.1093/mnras/85.1.2

Jura, M., Farihi, J., & Zuckerman, B. 2007, The Astrophysical Journal, 663, 1285, doi: 10.1086/518767

Koester, D., Gänsicke, B. T., & Farihi, J. 2014, Astronomy & Astrophysics, Volume 566, id.A34, <NUMPAGES>20</NUMPAGES> pp., 566, A34, doi: 10.1051/0004-6361/201423691

Kratter, K. M., & Perets, H. B. 2012, The Astrophysical Journal, 753, 91, doi: 10.1088/0004-637X/753/1/91

Kuchner, M. J., & Brown, M. E. 2000, Publications of the Astronomical Society of the Pacific, 112, 827, doi: 10.1086/316581

Lucas, M., & Bottom, M. 2020, Journal of Open Source Software, 5, 2843, doi: 10.21105/joss.02843

Luhman, K. L., Burgasser, A. J., & Bochanski, J. J. 2011, The Astrophysical Journal, 730, L9, doi: 10.1088/2041-8205/730/1/L9

Marley, M., Saumon, D., Morley, C., et al. 2021a, Sonora Bobcat: cloud-free, substellar atmosphere models, spectra, photometry, evolution, and chemistry, Zenodo, doi: 10.5281/zenodo.5063476

Marley, M. S., Saumon, D., Visscher, C., et al. 2021b, The Astrophysical Journal, 920, 85, doi: 10.3847/1538-4357/ac141d

Marois, C., Lafrenière, D., Doyon, R., Macintosh, B., & Nadeau, D. 2006, The Astrophysical Journal, 641, 556, doi: 10.1086/500401

Mawet, D., Milli, J., Wahhaj, Z., et al. 2014, ApJ, 792, 97, doi: 10.1088/0004-637X/792/2/97

Mustill, A. J., & Villaver, E. 2012, The Astrophysical Journal, 761, 121, doi: 10.1088/0004-637X/761/2/121

Nordhaus, J., & Spiegel, D. S. 2013, Monthly Notices of the Royal Astronomical Society, 432, 500, doi: 10.1093/mnras/stt569

Pairet, B. 2020, PhD thesis, UCL - Université Catholique de Louvain. https://dial.uclouvain.be/pr/boreal/object/boreal:240621

Pairet, B., Cantalloube, F., Gomez Gonzalez, C. A., Absil, O., & Jacques, L. 2019a, Monthly Notices of the Royal Astronomical Society, 487, 2262, doi: 10.1093/mnras/stz1350

Pairet, B., Cantalloube, F., & Jacques, L. 2019b, arXiv:1812.01333 [astro-ph]. http://arxiv.org/abs/1812.01333

—. 2020, arXiv:2008.05170 [astro-ph]. http://arxiv.org/abs/2008.05170

Pathak, P., de la Roche, D. J. M. P. d., Kasper, M., et al. 2021, arXiv:2104.13032 [astro-ph]. http://arxiv.org/abs/2104.13032

Perets, H. B. 2010, arXiv e-prints, arXiv:1001.0581. https://ui.adsabs.harvard.edu/abs/2010arXiv1001.0581P

—. 2011, 1331, 56, doi: 10.1063/1.3556185

Perets, H. B., & Kratter, K. M. 2012, The Astrophysical Journal, 760, 99, doi: 10.1088/0004-637X/760/2/99

Phillips, M. W., Tremblin, P., Baraffe, I., et al. 2020, Astronomy and Astrophysics, 637, A38, doi: 10.1051/0004-6361/201937381

Ren, B., Pueyo, L., Zhu, G. B., Debes, J., & Duchêne, G. 2018, The Astrophysical Journal, 852, 104, doi: 10.3847/1538-4357/aaa1f2

Schatzman, E. 1945, Annales d'Astrophysique, 8, 143. https://ui.adsabs.harvard.edu/abs/1945AnAp....8..143S

Schroeder, D. J., Golimowski, D. A., Brukardt, R. A., et al. 2000, The Astronomical Journal, 119, 906, doi: 10.1086/301227

Serabyn, E., Huby, E., Matthews, K., et al. 2017, The Astronomical Journal, 153, 43, doi: 10.3847/1538-3881/153/1/43

Skemer, A. J., & Close, L. M. 2011, The Astrophysical Journal, 730, 53, doi: 10.1088/0004-637X/730/1/53

Soummer, R., Pueyo, L., & Larkin, J. 2012, The Astrophysical Journal Letters, 755, L28, doi: 10.1088/2041-8205/755/2/L28

Spiegel, D. S., & Burrows, A. 2012, The Astrophysical Journal, 745, 174, doi: 10.1088/0004-637X/745/2/174

Takeda, Y. 2020, Monthly Notices of the Royal Astronomical Society, 499, 1126, doi: 10.1093/mnras/staa2869

Thalmann, C., Usuda, T., Kenworthy, M., et al. 2011, The Astrophysical Journal, 732, L34, doi: 10.1088/2041-8205/732/2/L34

Traub, W. A., & Oppenheimer, B. R. 2010, Exoplanets, 111. http://adsabs.harvard.edu/abs/2010exop.book..111T

van Dam, M. A., Bouchez, A. H., Le Mignant, D., et al. 2006, Publications of the Astronomical Society of the Pacific, 118, 310, doi: 10.1086/499498

van Dokkum, P. G. 2001, Publications of the Astronomical Society of the Pacific, 113, 1420, doi: 10.1086/323894

Vanderburg, A., Rappaport, S. A., Xu, S., et al. 2020, Nature, 585, 363, doi: 10.1038/s41586-020-2713-y

Veras, D. 2016, Royal Society Open Science, 3, 150571, doi: 10.1098/rsos.150571

Vigan, A., Gry, C., Salter, G., et al. 2015, Monthly Notices of the Royal Astronomical Society, 454, 129, doi: 10.1093/mnras/stv1928

Walt, S. v. d., Schönberger, J. L., Nunez-Iglesias, J., et al. 2014, PeerJ, 2, e453, doi: 10.7717/peerj.453

Wizinowich, P. L., Acton, D. S., Lai, O., et al. 2000, 4007, 2, doi: 10.1117/12.390368

Xu, S., Ertel, S., Wahhaj, Z., et al. 2015, Astronomy & Astrophysics, Volume 579, id.L8, <NUMPAGES>5</NUMPAGES> pp., 579, L8, doi: 10.1051/0004-6361/201526179

Xu, S., & Jura, M. 2012, The Astrophysical Journal, 745, 88, doi: 10.1088/0004-637X/745/1/88

Yelda, S., Lu, J. R., Ghez, A. M., et al. 2010, The Astrophysical Journal, Volume 725, Issue 1, pp. 331-352 (2010)., 725, 331, doi: 10.1088/0004-637X/725/1/331

Zuckerman, B., Melis, C., Klein, B., Koester, D., & Jura, M. 2010, The Astrophysical Journal, 722, 725, doi: 10.1088/0004-637X/722/1/725

APPENDIX

A. ADI PROCESSING RESULTS

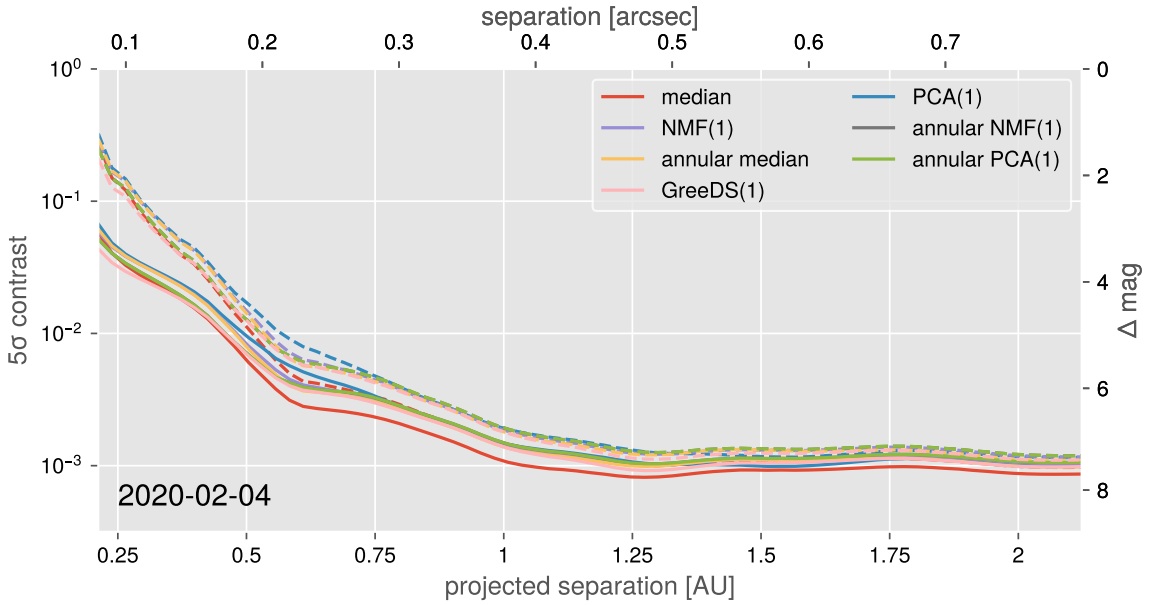

Figure 7. 5σ contrast curves from every ADI algorithm for the first epoch. Both the Gaussian (solid lines) and Student-t corrected (dashed lines) contrast curves are shown.

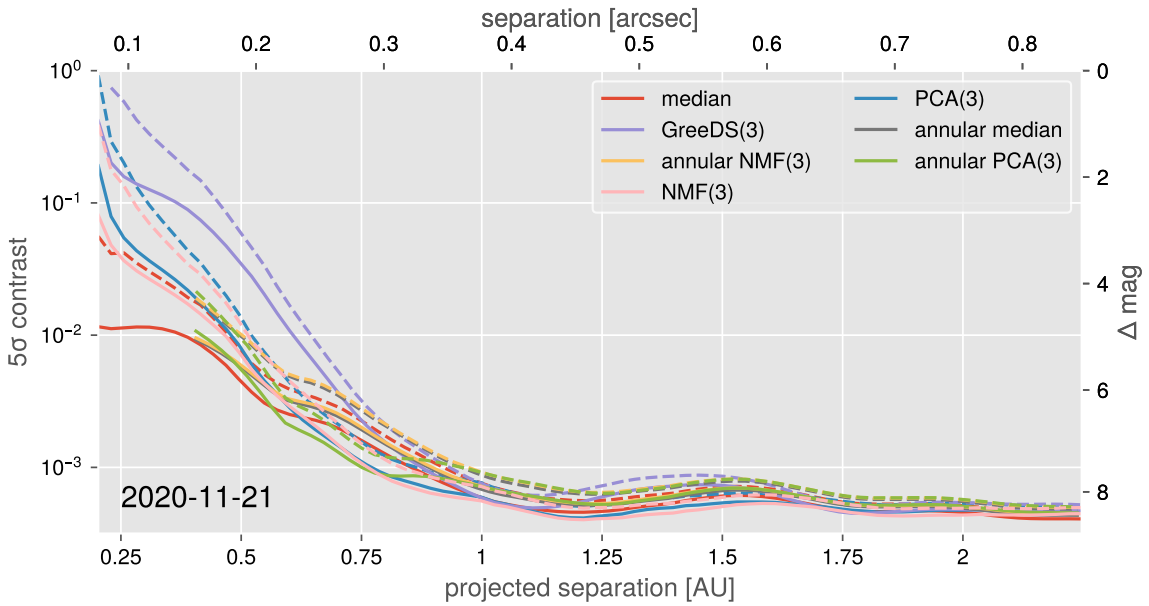

Figure 8. 5σ contrast curves from every ADI algorithm for the second epoch. Both the Gaussian (solid lines) and Student-t corrected (dashed lines) contrast curves are shown.

Fig. Set 10. ADI processing results

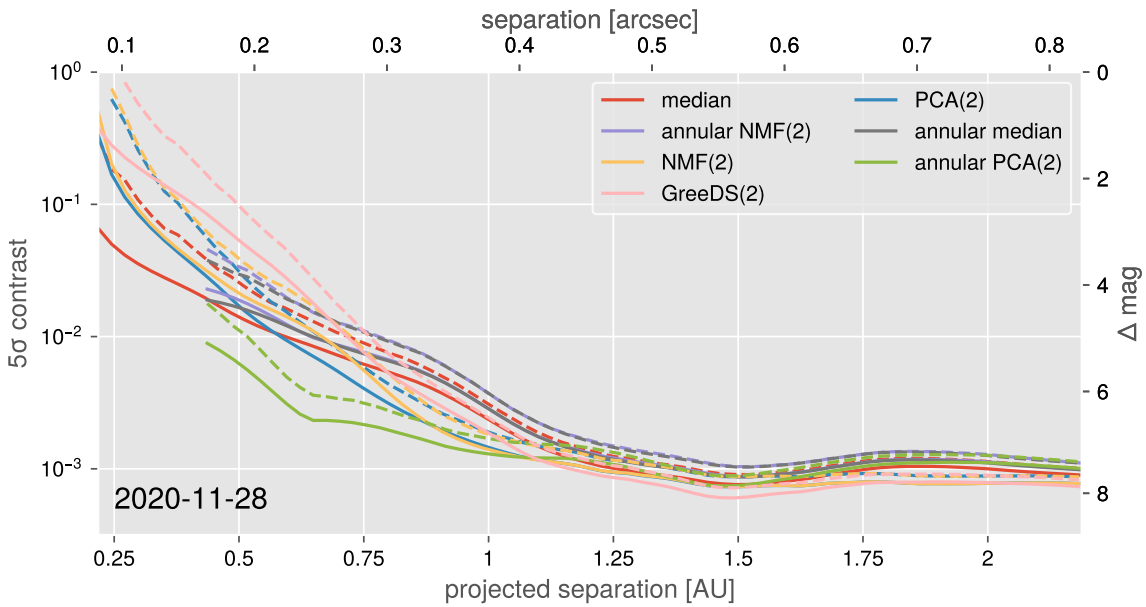

Figure 9. 5σ contrast curves from every ADI algorithm for the third epoch. Both the Gaussian (solid lines) and Student-t corrected (dashed lines) contrast curves are shown.

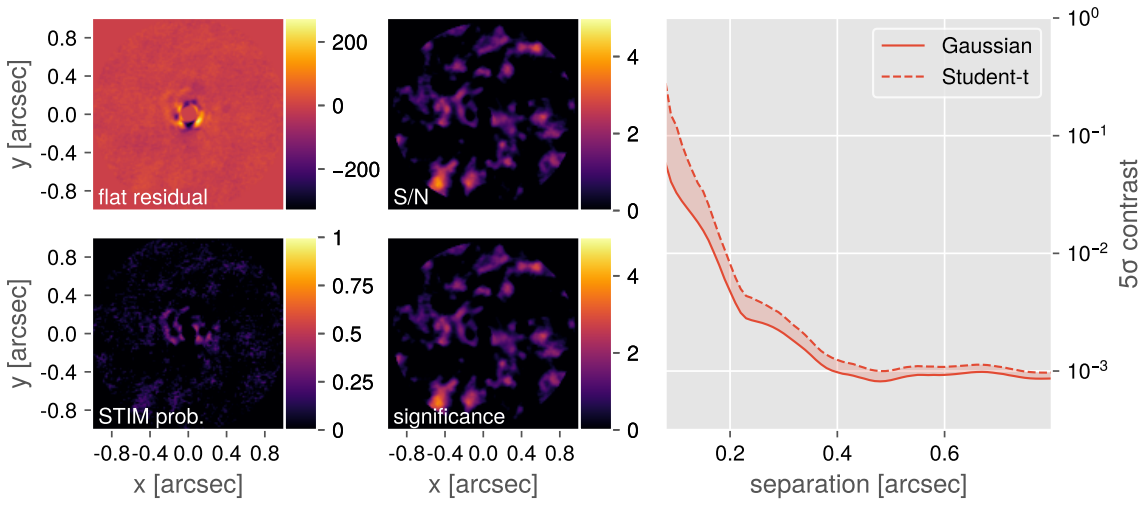

Figure 10. Post-processing results from the second epoch using full-frame median subtraction. The top-left frame is the collapsed residual frame, the top-right is the Gaussian S/N map, the bottom-left is the STIM probability map, and the bottom-right is the Student-t corrected significance map. In each frame the inner two FWHMs are masked out. The right figure show the Gaussian (solid line) and Student-t corrected (dashed curve) 5σ contrast curve. Outputs for other epochs and other algorithms (21 figures) are in the online figure set and the GitHub repository.

Fig. Set 11. PCA, NMF, and GreeDS mosaics

Fig. Set 12. PCA, NMF, and GreeDS results

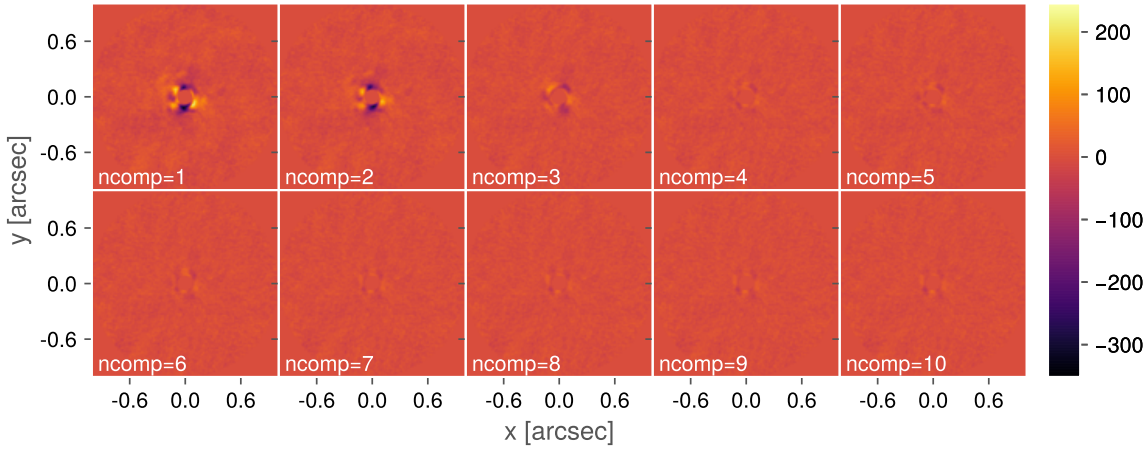

Figure 11. Collapsed residual frames from the first epoch using PCA reduction with 1-10 components. The figures share a common scale and the inner two FWHMs are masked out for all the frames. Outputs for the other epochs and for the NMF and GreeDS algorithms (9 figures) are in the online figure set and the GitHub repository

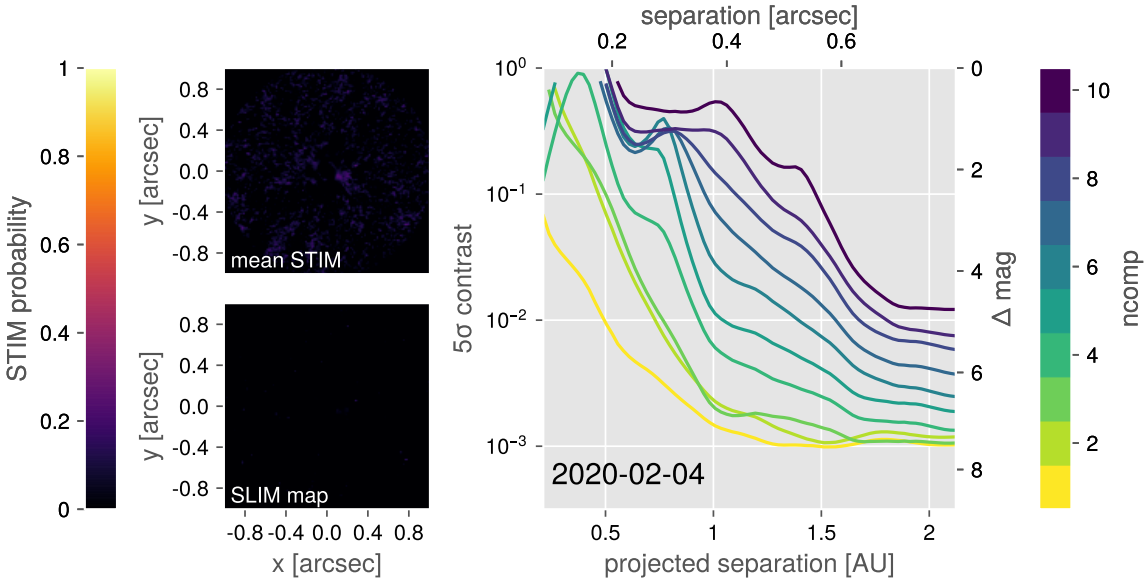

Figure 12. 5σ Gaussian contrast curves for the first epoch using PCA reduction with 1-10 components. The left two figures are the average STIM probability map, and the SLIM detection map. For both of these maps, a typical cutoff value is 0.5. Outputs for the other epochs and for the NMF and GreeDS algorithms (9 figures) are in the online figure set and the GitHub repository.

B. PROVISIONAL ORBIT FITTING

We found multiple interesting blobs in the reduced data that were not statistically significant. Nonetheless, we tried fitting Keplerian orbits using OFTI to determine the feasibility of the blobs being real companions. We began by estimating the astrometry of the blobs by eye in reduced data (Table 3, Figure 13). We tried simulating 10^4 orbits via rejection sampling with OFTI but no generated orbit was able to constrain all three points. Overall we determine these blobs are not real companions and are most likely systematic noise in the stellar PSF.

Table 3. Provisional astrometry for a blob of interest from each epoch. The separation and offset are in relation to Sirius B. The uncertainties are derived from the FWHM of the PSF from each epoch.

Date observed	offset (mas)	PA (°)
2020-02-04	123 ± 40	-128 ± 20
2020-11-21	119 ± 38	68 ± 18
2020-11-28	132 ± 41	37 ± 21

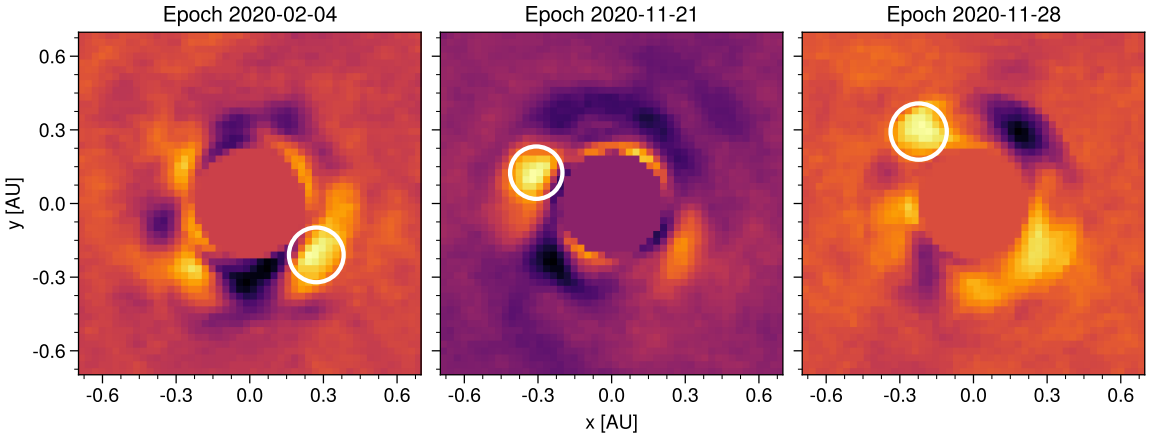

Figure 13. Provisional astrometry (white circles) displayed on collapsed and derotated residuals from each epoch. Each frame was cropped to the inner ∼0.7 AU (0.25″) and the inner two FWHMs have been masked out. The width of the circles represents the measurement uncertainty.